Simulating acoustic scattering from atmospheric temperature fluctuations using a *k*-space method

Jonathan A. Hargreaves,[a] Paul Kendrick, and Sabine von Hünerbein
Acoustics Research Centre, The University of Salford, Manchester M5 4WT, United Kingdom.

(Received 3 May 2013; revised 5 November 2013; accepted 8 November 2013)

This paper describes a numerical method for simulating far-field scattering from small regions of inhomogeneous temperature fluctuations. Such scattering is of interest since it is the mechanism by which acoustic wind velocity profiling devices (Doppler SODAR) receive backscatter. The method may therefore be used to better understand the scattering mechanisms in operation and may eventually provide a numerical test-bed for developing improved SODAR signals and post-processing algorithms. The method combines an analytical incident sound model with a *k*-space model of the scattered sound close to the inhomogeneous region and a near-to-far-field transform to obtain far-field scattering patterns. Results from two test case atmospheres are presented: one with periodic temperature fluctuations with height and one with stochastic temperature fluctuations given by the Kolmogorov spectrum. Good agreement is seen with theoretically predicted far-field scattering and the implications for multi-frequency SODAR design are discussed. © *2014 Acoustical Society of America* [http://dx.doi.org/10.1121/1.4835955]

PACS number(s): 43.28.Js, 43.28.Gq, 43.20.Fn, 43.20.Px [VEO] Pages: 83–92

I. INTRODUCTION

Sound Detection and Ranging (SODAR) devices measure the backscattering of sound pulses transmitted into the lower atmosphere, allowing remote sensing of a variety of data including inversion layers and vertical profiling, wind speed, wind direction, turbulence quantities and stability classes.[1] Unlike direct measurement techniques (such as mast anemometers), they are quick to deploy and provide continuous data with height; hence, they find application in atmospheric research, pollution monitoring, and wind-energy surveying.

In profiling the lower atmosphere using SODAR, one may encounter difficulties with range and velocity resolution as well as signal to noise ratio problems. To improve the accuracy of these parameters, new signals and analysis methods need to be evaluated. This is difficult to achieve by experimentation, however, since the "true" atmospheric data required for comparison is not available and must be acquired either from similar instruments or other devices with their own limitations. Thus, there is a requirement for a SODAR simulator to inform on SODAR performance characteristics over a range of atmospheric conditions and this paper presents some initial steps toward that objective. In addition, it studies whether the process causing the backscatter is compatible with the matched-filter post-processing required for multi-frequency "pulse compression" SODAR signals.[2,3] These have been proposed to overcome the usual tradeoff between transmitted power and height resolution by transmitting multiple pulses of different frequencies.

Atmospheric scattering from acoustic pulses is strongest where the spacing of the scattering structures is related to integer multiples of half a wavelength; the mechanism in operation here is Bragg scattering, though it has also been called "Acoustic Iridescence" in other applications.[4] Previous models of wind profilers have not simulated the scattering process directly but have been based on statistical models of the effective cross-section of sound scattering in the atmosphere,[1,5–7] ensemble average spectra of backscattered sound,[8] or frequency modulation of a pure tone by a simulated velocity profile.[9] In contrast, numerical algorithms such at Finite-Difference-Time-Domain (FDTD) can directly model the scattering of these transient acoustic pulses by a specific temperature and velocity distribution.[10–12] Given however that SODARs generally operate in the frequency range 1000–5000 Hz and generally have a range of 100 m upward, FDTD simulation of the entire scattering volume in three dimensions is unfortunately not feasible with currently available computing power.

The classical theory studies the scattering from a region of turbulence within an otherwise homogeneous atmosphere (for example, see Ref. 7, Sec. 7.1.1). The distance from the scattering volume to the sound source and receivers is assumed to be large with respect to the characteristic size of the volume, so the incident sound wave is approximately a plane wave and a far-field approximation may also be applied to the scattered sound at the receivers. Cheinet *et al.*[13] recently studied this scenario numerically in two dimensions (2D) using FDTD. Good agreement with the classical theory was seen for large scattering angles and the discrepancies at small scattering angles could be explained by approximations introduced in the classical theory.

In this paper, a similar numerical study is conducted in three dimensions (3D), but requires a hybrid approach due to the significantly increased storage and computation requirements that 3D presents. In particular, it was possible for the authors of Ref. 13 to model in 2D (using a cluster) a domain large enough that the receivers could be placed in the far-field relative to the scattering volume and the far-field

[a]Author to whom correspondence should be addressed. Electronic mail: j.a.hargreaves@salford.ac.uk

scattering calculated directly. In contrast, the algorithm reported herein was both in 3D and designed to run on a single workstation, so the volume modeled using FDTD had to be restricted to be only slightly larger than the turbulent region. This meant far-field pressure could not be estimated directly from the grid data and instead a Near-To-Far-Field (NTFF) transform[14] was applied to convert the data at the edge of the grid into far-field pressure. Since the NTFF transform should operate only on the scattered sound, it was also necessary to separate the incident and scattered fields. Separate modeling of incident and scattered sound waves is not uncommon in acoustic and electromagnetic simulation of scattering from impenetrable objects[15] (see "scattered field" formulation Sec. 5.10), but its application to scattering by a region of inhomogeneous refractive index is believed to be novel.

The structure of the complete algorithm is depicted in Fig. 1, showing its three parts (which are spatially coincident but depicted separately for clarity). On the left is the incident sound model; this is stated analytically and propagates through V unchanged. In the middle is the scattered sound model in V; this provides a correction such that the total sound respects the inhomogeneous refractive index of V. Finally, on the right is the far-field scattered sound model, computed using the NTFF transform over a surface which is within the FDTD modeling domain but which also entirely encloses V. Compared to a total-field model of the entire atmosphere, this approach has the benefits of reduced computational cost, since it avoids using an expensive volumetric method to model the homogeneous part of the atmosphere, and better use of floating point precision, since the incident and scattered sound waves (which typically differ by many orders of magnitude) are computed separately so "subtraction error" will not occur.

The numerical method is described in detail in Sec. II and the results of the numerical simulations are presented in Sec. III. Sec. IV summarizes the findings of the paper, discusses the scope of the model and identifies future directions.

II. NUMERICAL METHOD

Consider the problem of a scattering volume V with an inhomogeneous temperature profile $T(\mathbf{r})$, where $\mathbf{r}$ is a vector representing position in 3D Cartesian space, within an otherwise homogenous atmosphere with temperature T_0, density ρ_0, and sound speed c_0. Density and sound speed within V may be found by $\rho(\mathbf{r}) = \rho_0 T_0/T(\mathbf{r})$ and $c(\mathbf{r}) = c_0\sqrt{T(\mathbf{r})/T_0}$, respectively, on the assumption that the ambient pressure is constant and the air is dry and obeys the ideal-gas law. It is assumed that the medium is stationary except for the small perturbations due to acoustic particle velocity (i.e., no wind or medium velocity due to turbulence).

An incident sound wave, which satisfies the wave equation with ρ_0 and c_0, propagates upward through the homogeneous atmosphere. As it impinges on V, the variations in density and sound speed cause changes in how the sound wave propagates, modifying its shape. Figure 2 illustrates an exaggerated case of this where the temperature in V (area within dotted circle) is significantly lower than T_0, causing the sound wave to slow down. Rather than modify the

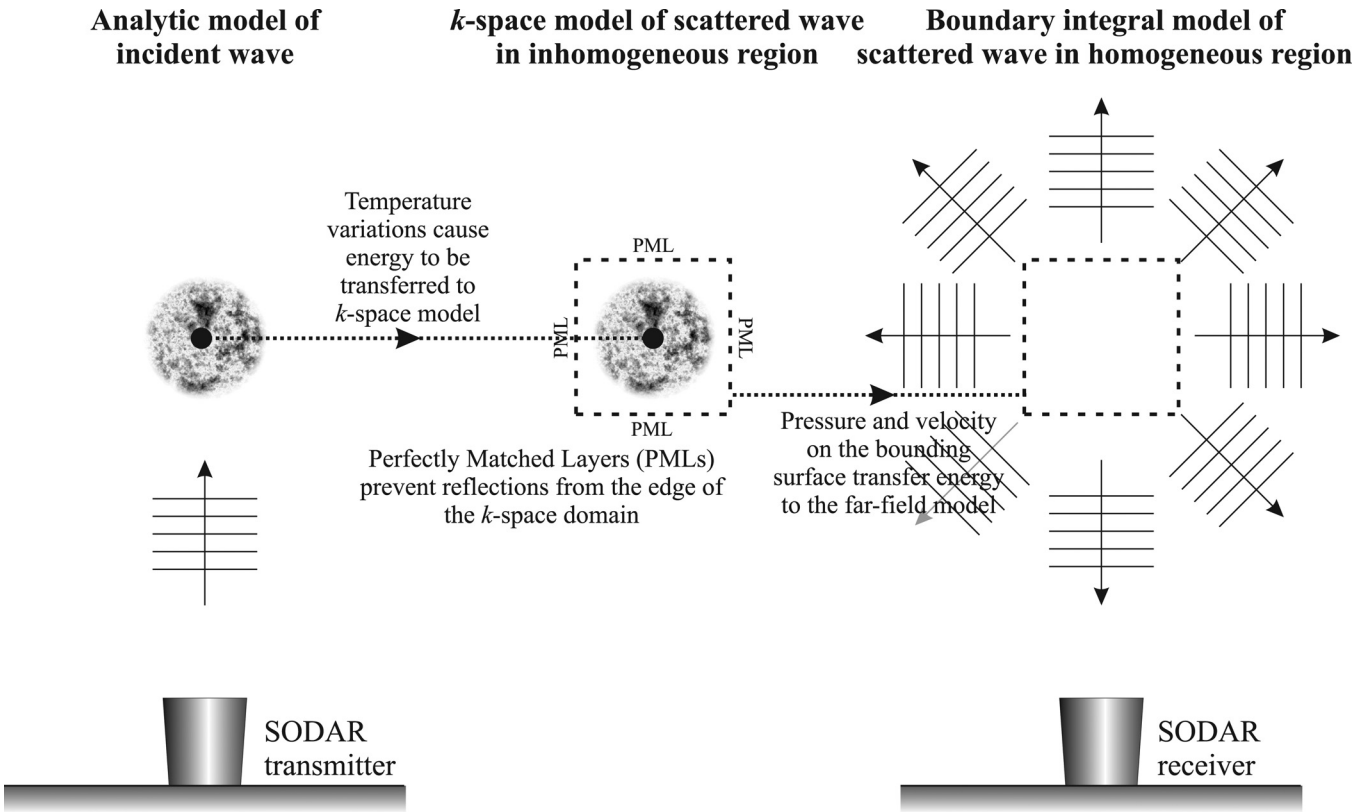

FIG. 1. Diagram illustrating the solution process of the incident plus scattered model. The incident sound is defined analytically. The scattered sound is modeled by a k-space scheme close to the inhomogeneous region and by a boundary integral equation further away.

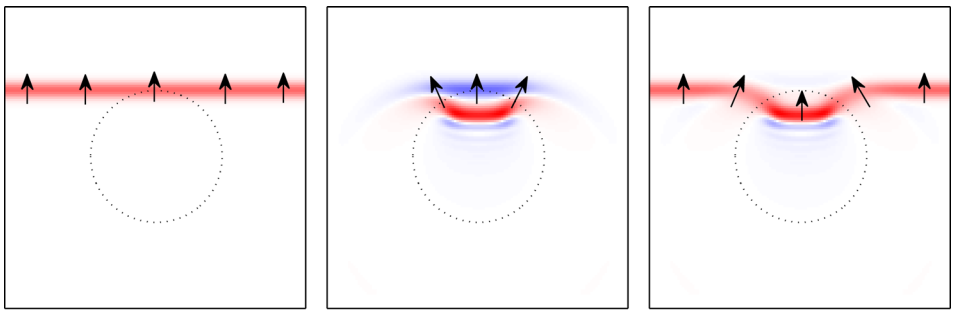

FIG. 2. (Color online) Example of the incident plus scattering model of a cold temperature region (inside the dashed circle) within a uniform temperature medium. Arrows indicate wave propagation direction and color scale is identical across all three subplots. (a) incident pressure; (b) scattered pressure; (c) total pressure (incident + scattered).

incident sound wave [Fig. 2(a)], the algorithm instead introduces a scattered sound wave [Fig. 2(b)] such that the sum of these gives a total sound wave [Fig. 2(c)], which satisfies the wave equation with $\rho(\mathbf{r})$ and $c(\mathbf{r})$. This includes cancellation of the incident and scattered wavefronts immediately above the cold region such that "slowing" of the total wave can be observed. Ultimately, it is desirable to know the directivity with which this scattered sound wave propagates into the far-field after it leaves V; this is calculated using a boundary integral over a surface enclosing V.

A. Incident sound model

The homogeneous incident sound wave is chosen to be a plane wave with its propagation direction described by the unit vector $\hat{\mathbf{k}}_i$ and time variation by the function $f(\tau)$. Its pressure p_i and particle velocity $\boldsymbol{u}_i$ are given by

$$p_i(\mathbf{r},t) = f\left(t - \hat{\mathbf{k}}_i \cdot \mathbf{r}/c_0\right), \tag{1}$$

$$\boldsymbol{u}_i(\mathbf{r},t) = \hat{\mathbf{k}}_i p_i(\mathbf{r},t)/\rho_0 c_0. \tag{2}$$

These satisfy the first-order linearized equations for a homogeneous medium

$$\rho_0 \frac{\partial \boldsymbol{u_i}}{\partial t} = -\nabla p_i, \tag{3}$$

$$\frac{\partial p_i}{\partial t} = -\rho_0 c_0^2 \nabla \cdot \boldsymbol{u_i}. \tag{4}$$

B. Scattered sound model

The scattered sound wave has pressure p_s and particle velocity $\boldsymbol{u}_s$. Below are the first order linearized equations for an inhomogeneous medium [e.g., Ref. 13 Eq. (1) and Eq. (2), omitting source and medium velocity terms], which apply to the total pressure $p_t = p_i + p_s$ and total particle velocity $\boldsymbol{u}_t = \boldsymbol{u}_i + \boldsymbol{u}_s$ inside V,

$$\rho(\mathbf{r}) \frac{\partial \boldsymbol{u}_t}{\partial t} = -\nabla p_t, \tag{5}$$

$$\frac{\partial p_t}{\partial t} = -\rho(\mathbf{r}) c^2(\mathbf{r}) \nabla \cdot \boldsymbol{u}_t. \tag{6}$$

These are split into the incident and scattered parts

$$\rho(\mathbf{r}) \left(\frac{\partial \boldsymbol{u_i}}{\partial t} + \frac{\partial \boldsymbol{u_s}}{\partial t} \right) = -(\nabla p_i + \nabla p_s), \tag{7}$$

$$\frac{\partial p_i}{\partial t} + \frac{\partial p_s}{\partial t} = -\rho(\mathbf{r}) c^2(\mathbf{r}) (\nabla \cdot \boldsymbol{u_i} + \nabla \cdot \boldsymbol{u_s}). \tag{8}$$

Subtracting Eq. (3) from Eq. (7) and Eq. (4) from Eq. (8) gives the equations to be modeled numerically

$$\rho(\mathbf{r}) \frac{\partial \boldsymbol{u_s}}{\partial t} = -\nabla p_s + (\rho_0 - \rho(\mathbf{r})) \frac{\partial \boldsymbol{u_i}}{\partial t}, \tag{9}$$

$$\begin{aligned} \frac{\partial p_s}{\partial t} &= -\rho(\mathbf{r}) c^2(\mathbf{r}) \nabla \cdot \boldsymbol{u_s} + \left(\rho_0 c_0^2 - \rho(\mathbf{r}) c^2(\mathbf{r})\right) \nabla \cdot \boldsymbol{u_i} \\ &= -\rho_0 c_0^2 \nabla \cdot \boldsymbol{u_s}. \end{aligned} \tag{10}$$

It should be noted that p_s and $\boldsymbol{u_s}$ include multiple scattering as well as compensation for the first-order scattering that p_i and $\boldsymbol{u_i}$ should experience due to $\rho(\mathbf{r})$ and $c(\mathbf{r})$; Eq. (9) and Eq. (10) are exact results. The simplification in the second line of Eq. (10) is possible because $\rho(\mathbf{r})c^2(\mathbf{r}) = \rho_0 c_0^2$ when only temperature fluctuations are present, hence the incident term equates to zero and may be omitted. From the perspective of the scattered sound model the term $\partial \boldsymbol{u_i}/\partial t$ in Eq. (9) is like a distributed source, passing sound energy from the incident sound model to the scattered sound model such that the total sound (sum of incident and scattered) satisfies the inhomogeneous medium properties in V.

C. *k*-space algorithm

For an incident plus scattered sound model to operate correctly, it is crucial that the speed of wave propagation is identical in both models; if not, then sound energy being transferred from the incident to scattered model in the current time-step will be misaligned with scattering from previous time-steps. This is automatically assured in typical "scattered field" FDTD formulations, since a FDTD scheme is also used for the incident sound. However, further consideration is required here because the incident sound wave is stated analytically. Standard FDTD algorithms suffer from the well reported issue of numerical dispersion (e.g., Ref. 15, Chap. 4), meaning the speed of wave propagation is direction and frequency dependent, so they are unsuitable for this application. Here instead the scattered field in the homogeneous volume will be evaluated using a *k*-space variant of the FDTD method.[16] This is closely related to the Pseudo-Spectral-Time-Domain (PSTD)[17] method and uses a spatial

Fourier series to interpolate the grid data at each time-step, allowing the spatial derivatives to be found by Fast Fourier Transform (FFT) using fewer grid points per wavelength than would be required by a finite-difference scheme of similar precision. Crucially for the application herein, numerical dispersion effects are compensated for in the k-space spatial operators (see Ref. 16, Sec. II), so the resulting algorithm is free of numerical dispersion.

The algorithm used here has been adapted from Tabei *et al.*[16] and the k-wave toolbox[18] with the following primary differences: inclusion of the extra incident sound terms above, absence of relaxation absorption, and the use of collocated (non-staggered) grids. Use of collocated grids is known to create spatial Gibbs effects for sudden changes in medium properties, but those are not present in the atmospheric temperature profiles under consideration so the algorithm can benefit from a slightly simpler NTFF implementation and the potential to support velocity fluctuations in future (these involve spatial tensor derivatives which are complicated to implement on staggered grids). The pressure and particle velocity grids are however still staggered in time. For a collocated grid scheme the k-space differential operators, including dispersion correction, are given by the following concatenation of operators, where $\mathcal{F}$ represents a multi-dimensional FFT and $\mathcal{F}^{-1}$ its inverse. Here Δ_t is the time-step duration, k is the spatial wave number in the k-domain (for more details see Ref. 16) and k_x is its component in the x direction. Note that for brevity only the x direction operators are given in what follows, but equivalent statements exist for y and z,

$$\frac{\partial}{\partial x}\{\ldots\} \equiv \mathcal{F}^{-1}\left\{ik_x \mathrm{sinc}(c_0\Delta_t k/2)\mathcal{F}\{\ldots\}\right\}. \tag{11}$$

The collocated grid algorithm was verified against the staggered algorithm implemented in the k-wave toolbox by marching on from initial conditions, and the error between the two algorithms was found to be less than -50 dB compared to the excited pressure in the medium.

The modeling region is surrounded by a Perfectly Matched Layer (PML). This is particularly critical since it prevents both reflections from the edge of the domain and wrap-around due to the FFT. It is also implemented according to Ref. 16 but with the significant simplification that relaxation absorption is absent, hence the derivation is repeated here. In order to implement the PML, the scattered pressure must be split into directional components $p_s = p_s^x + p_s^y + p_s^z$. This decomposes Eq. (9) and Eq. (10) into a set of coupled (via p_s) 1D equations in which PMLs may be applied by replacing each time differential with a first-order differential equation involving a dimensionless absorption parameter α_x,

$$\begin{aligned}\frac{\partial u_s^x}{\partial t}(\mathbf{r},t) &\rightarrow \frac{\partial u_s^x}{\partial t}(\mathbf{r},t) + \alpha_x(\mathbf{r})u_s^x(\mathbf{r},t),\\ \frac{\partial p_s^x}{\partial t}(\mathbf{r},t) &\rightarrow \frac{\partial p_s^x}{\partial t}(\mathbf{r},t) + \alpha_x(\mathbf{r})p_s^x.\end{aligned} \tag{12}$$

Yuan *et al.*[19] showed that if such equations with the form $\partial f/\partial t + \alpha f = g$ are replaced by ones with the form $\partial(e^{\alpha t}f)/\partial t = e^{\alpha t}g$ then larger attenuations are possible without numerical instability. This time derivative may be approximated by central finite difference giving $e^{\alpha\Delta_t/2}f(t^+) - e^{-\alpha\Delta_t/2}f(t^-) = \Delta_t g(t)$. The time differentials above are therefore approximated by the following statements, which simplify to the regular central difference scheme, where $\alpha_x = 0$,

$$\begin{aligned}&\frac{\partial u_s^x}{\partial t}(\mathbf{r},t) + \alpha_x(\mathbf{r})u_s^x(\mathbf{r},t)\\ &\quad\approx \frac{e^{\alpha_x(\mathbf{r})\Delta_t/2}u_s^x(\mathbf{r},t+\Delta_t/2) - e^{-\alpha_x(\mathbf{r})\Delta_t/2}u_s^x(\mathbf{r},t-\Delta_t/2)}{\Delta_t},\\ &\frac{\partial p_s^x}{\partial t}(\mathbf{r},t) + \alpha_x(\mathbf{r})p_s^x(\mathbf{r},t)\\ &\quad\approx \frac{e^{\alpha_x(\mathbf{r})\Delta_t/2}p_s^x(\mathbf{r},t+\Delta_t/2) - e^{-\alpha_x(\mathbf{r})\Delta_t/2}p_s^x(\mathbf{r},t-\Delta_t/2)}{\Delta_t}.\end{aligned} \tag{13}$$

The absorption parameters are tapered in the PML according to

$$\alpha_x = A\frac{c_0}{\Delta_x}\left(\frac{x-x_0}{x_1-x_0}\right)^4. \tag{14}$$

Here x_0 is the coordinate at the inner edge of the PML, x_1 is the coordinate of the outer edge of the grid, and A is the absorption per cell in nepers. So long as $\rho(\mathbf{x}) = \rho_0$ and $c(\mathbf{x}) = c_0$ in the PML zone, then no energy will be transferred here and no further consideration need to be made to the effect of the incident terms on the PML. The PML implementation was verified using Yuan *et al.* approach[19] of comparing a small domain model to a larger domain model; error due to PML artifacts was found to be around -60 dB compared to the excited pressure in the medium.

D. Near-to-far-field transform

The NTFF transform is concerned with mapping the scattered sound in the near-field to plane waves in the far-field. This begins with the time domain Kirchhoff–Helmholtz integral equation[20] on a surface S (enclosing V) which calculates the pressure $p_s(\mathbf{r},t)$ scattered to a point $\mathbf{r}$ outside S due to the pressure field $p(\mathbf{r}',t)$ on S,

$$\begin{aligned}p_s(\mathbf{r},t) = \int_S\int \hat{\mathbf{n}}\cdot[&p(\mathbf{r}',t)*\nabla g(\mathbf{r},\mathbf{r}',t)\\ &- g(\mathbf{r},\mathbf{r}',t)*\nabla p(\mathbf{r}',t)]d\mathbf{r}'.\end{aligned} \tag{15}$$

Here $*$ represents temporal convolution and the gradient is taken with respect to $\mathbf{r}'$. Point $\mathbf{r}'$ lies on S, $\hat{\mathbf{n}}$ is the surface-normal unit vector at $\mathbf{r}'$, and $g(\mathbf{r},\mathbf{r}',t) = \delta(t-R/c_0)/4\pi R$ is the time domain Green's function with $R = |\mathbf{r}-\mathbf{r}'|$.

The NTFF transform is found from Eq. (15) by applying a far-field approximation; this assumes that $\mathbf{r}'$ and $\mathbf{r}$ are, respectively, near and far from the origin of the coordinate system so R may be approximated by $R \approx |\mathbf{r}| - \hat{\mathbf{r}}\cdot\mathbf{r}'$. The Green's function is modified, with spherical spreading and propagation delay $|\mathbf{r}|/c_0$ from the origin to $\mathbf{r}$ being compensated for, leading to a far-field Green's function $g_{ff}(\hat{\mathbf{r}},\mathbf{r}',t) = \delta(t+\hat{\mathbf{r}}\cdot\mathbf{r}'/c_0)$ in

direction $\hat{\mathbf{r}}$. Substituting this Eq. (15) allows the far-field pressure $p_{ff}(\hat{\mathbf{r}},t)$ in direction $\hat{\mathbf{r}}$ to be computed,

$$p_{ff}(\hat{\mathbf{r}},t) = \int_S\int \hat{\mathbf{n}}\cdot\left[p(\mathbf{r}',t)*\nabla g_{ff}(\hat{\mathbf{r}},\mathbf{r}',t) - g_{ff}(\hat{\mathbf{r}},\mathbf{r}',t)*\nabla p(\mathbf{r}',t)\right]d\mathbf{r}'. \quad (16)$$

By applying the sifting property of the delta function it may be shown that $p(\mathbf{r}',t)*\nabla g_{ff}(\hat{\mathbf{r}},\mathbf{r}',t) = \hat{\mathbf{r}}\partial p/\partial t(\mathbf{r}',t')/c_0$ and $g_{ff}(\hat{\mathbf{r}},\mathbf{r}',t)*\nabla p(\mathbf{r}',t) = \nabla p(\mathbf{r}',t')$, where $t' = t + \hat{\mathbf{r}}\cdot\mathbf{r}'/c_0$. Substituting this and Eq. (5) [with $\rho(\mathbf{r}') = \rho_0$ since $\mathbf{r}'$ is outside V] produces

$$p_{ff}(\hat{\mathbf{r}},t) = \int_S\int \frac{\partial}{\partial t}\hat{\mathbf{n}}\cdot\left[\hat{\mathbf{r}}p(\mathbf{r}',t')/c_0 + \rho_0\boldsymbol{u}(\mathbf{r}',t')\right]d\mathbf{r}'. \quad (17)$$

In practice, S is chosen to be the surface of a cube aligned to the k-space grid just inside the PML. The spatial integral is performed numerically using the trapezium rule with abscissa collocated with the k-space grid points, so no spatial interpolation is required for this collocated-grid scheme. However, the time-retardation/advancement implicit in t' is not typically an integer multiple of Δ_t so temporal interpolation is required. In accordance with the temporal finite-difference operators used in the update equations, the grid pressure and velocity components are interpolated linearly between time-steps using triangle functions.

Here a choice presents itself. The temporal derivative in Eq. (17) can either be applied directly to the triangle functions (as was done by Luebbers *et al.*[14]) or moved outside the surface integral and evaluated by finite difference. A consequence of the former approach is that the quantities inside the integral are piece-wise constant instead of piece-wise linear, meaning the retardation is less well approximated (effectively rounded to the nearest time-step). This produces a simpler algorithm with reduced storage requirements. However, numerical experiments showed that accuracy is reduced compared with the approach of moving the temporal derivative outside the integral; hence, this latter approach is chosen.

Because Eq. (17) involves a time-advancement operator, evaluating the current instantaneous far-field pressure requires past and future grid data. Instead of storing the time history of the grid data, which would be prohibitively large, the algorithm instead maintains a buffer of the far-field components, starting from zero initial conditions and adding grid data as it becomes available; a similar approach was implemented by Luebbers *et al.*[14] The geometric and quadrature weights associated with each grid point were pre-calculated; this represents a significant storage requirement, but the alternative, re-computing the coefficients at every iteration, is extremely inefficient on a CPU (though it may be an appropriate strategy if the code was implemented on a GPGPU).

The NTFF implementation was verified by calculating the grid data analytically as if there was a point source located at the center of the grid, substituting that into the NTFF algorithm and comparing the output to the analytically calculated far-field pattern. Normalized mean square error between the numerical and analytical results was −24 dB and the angular variation of the far-field pressure was only ±0.02 dB (indicating the orientation of S does not affect the NTFF output). Taflove[15] identified that NTFF implementations may also be compromised by incomplete cancelation of the monopole and dipole terms in the boundary integral, radiating significant energy at 180° from its intended far-field direction (i.e., back through the medium and out the other side), and recommends removing sections of S, which are not expected to contribute to the far-field angle under consideration. However, numerical experiments showed that this was not an issue for the NTFF implementation given here; a scenario with strong forward scattering (similar to Fig. 2) was simulated and the erroneous backscatter off the top surface was −58 dB compared to the correct forward-scatter, which is the same error magnitude as caused by PML reflections. It is therefore concluded that the far-field pressure numerical "signal to noise ratio" (with respect to scattering angle) of this algorithm is approximately 60 dB.

III. RESULTS OF SCATTERING FROM ATMOSPHERES

In this section, some acoustic scattering results from temperature fluctuations simulated using the new numerical model are presented. Sections III A and III B investigate scattering from periodic and stochastic temperature fluctuations, respectively. A secondary aim of this investigation is to predict the performance of multi-frequency SODAR systems. To this end the phase coherence of backscatter from temperature fluctuations typical of atmospheric turbulence will be investigated, since this has been shown to affect the performance of the matched-filter post-processing they utilize.[21] Modeling temperature fluctuations only is acceptable to give a first insight into this phenomenon, since classical theory asserts that turbulent movement of the medium does not cause backscatter and that the effect of humidity on scattering cross-section is not significant over dry ground (Ref. 7, Sec. 7.1.4). The parameters for the homogeneous part of the atmosphere are taken to be[22] $T_0 = 288\,\mathrm{K} \approx 15\,^\circ\mathrm{C}$, $\rho_0 = 1.22\,\mathrm{kg/m^3}$, and $c_0 = 340\,\mathrm{m/s}$.

The grid dimensions were chosen to be $N_x = N_y = N_z = 256$, so each of the eight 3D double-precision arrays required to store the grid data occupied 128 MB, being 1 GB in total. The PML depth and absorption were chosen to be eight layers and 16 Nepers per layer, respectively; this is significantly thinner than used by Cheinet *et al.*[13] but is similar to the configuration recommended by Tabei *et al.*[16] and was found to be a good compromise to give minimum wrap-around or reflection at the boundaries of the numerical grid while maximizing the enclosed simulation volume. The grid-point spacing Δ_x was 2 cm in all dimensions giving a spatial Nyquist frequency of 8.5 kHz and a modeled volume of 4.8 m × 4.8 m × 4.8 m within the PMLs. This is significantly smaller than the 25 m radius area modeled by Cheinet *et al.*[13] but is still of interest because it is on the order of size of a SODAR "range gate" (the pulse duration divided by the speed of sound), the scattering by each of which is typically treated separately in SODAR post-processing.

To satisfy the stability criterion of the k-space method, the time-step duration Δ_t was set at 20 μs, giving a temporal

Nyquist frequency of 25 kHz and a Courant–Friedrichs–Lewy number $c_0\Delta_t/\Delta_x = 0.34$. These limits may at first seem quite conservative relative to the excitation pulse center frequency (mostly 1 kHz), but Bragg backscattering effects involve refractive index changes with as little as half the wavelength of the reflected sound, so a temperature fluctuation which reflects at 1 kHz may have a periodicity of around 0.17 m which equates to only 8.5 grid points per oscillation. Also, 360 far-field directions were modeled spaced at equal angles over the $y = 0$ plane.

The incident sound (as defined in Sec. II A) was chosen to be a modulated Gaussian plane wave traveling vertically upward, typical of a SODAR vertical beam, so $\hat{\mathbf{k}}_i = \hat{\mathbf{z}}$ and $f(\tau) = e^{-((\tau-\mu)/2\sigma)^2}\cos 2\pi f_m(\tau-\mu)$, where f_m is the modulation frequency and μ and σ are the pulse delay and duration (standard deviation) parameters, respectively. Unless stated otherwise $f_m = 1$ kHz, $\mu = 60$ ms, and $\sigma = 10$ ms, which are approximately representative of a SODAR pulse. In all cases, the temperature fluctuations were windowed to ensure that no incident terms [$\partial \boldsymbol{u}_i/\partial t$ in Eq. (9)] arose in the PML zone and that scattering cross-section was not influenced by the k-space domain shape. This was performed using a spherical flat-top (Tukey) window $w(\mathbf{r})$,

$$w(\mathbf{r}) = \begin{cases} 1, & |\mathbf{r}| < r_1 \\ \frac{1}{2} + \frac{1}{2}\cos\left(\frac{|\mathbf{r}| - r_1}{r_0 - r_1}\right), & r_1 \le |\mathbf{r}| \le r_0 \\ 0, & r_0 < |\mathbf{r}|. \end{cases} \quad (18)$$

The window's outer radius $r_0 = 2.4$ m unless stated otherwise and its inner radius $r_1 = (3/4)r_0$ in all cases. The scattering volume V_{scat} was estimated by performing a volume integral of $w(\mathbf{r})$, which for $r_0 = 2.4$ m evaluates as $V_{\text{scat}} = 39.2\ \text{m}^3$.

A. Atmosphere with periodic temperature fluctuations

It is widely accepted that the dominant backscattering mechanism in monostatic SODAR systems is Bragg scattering from temperature fluctuations with a spatial period that equals half the acoustic wavelength. Simulation of these fluctuations in isolation will be performed in this section to give increased understanding of this phenomenon.

The first set of simulations involved testing scattering regions of five different sizes, with radii logarithmically spaced fractions of the maximum window size, to characterize how the scattering pattern changes as the size of the fluctuating temperature field varies with wavelength. In these tests, a shorter pulse ($\sigma = 1$ ms) was chosen since its wider spectral peak made it possible to quantify the frequency response of the backscattering process. It should be noted that despite the fact that this pulse is very short, Bragg scattering will still occur since it is a linear mechanism defined by the medium properties, not by the excitation (for example, see the impulse response plots in Fig. 8 of Ref. 4). The spatial period and amplitude Δ_T of the temperature fluctuations were set to be half the acoustic wavelength at the modulation frequency of the pulse and 1 K, respectively; this will be referred to as a "Bragg Atmosphere,"

$$T(\mathbf{r}) = T_0 + w(\mathbf{r})\cos(4\pi f_m \hat{\mathbf{z}}\cdot\mathbf{r}/c)\Delta_T. \quad (19)$$

The far-field scattering results are shown in Fig. 3 and summarized in Table I. The radial quantity $H(\theta)$ in the polar plots is the scattered power ratio, being the power in the scattered sound normalized to the power density in the incident wave, expressed in dB. It is calculated by

$$H(\theta) = \frac{\sum_{m=-\infty}^{\infty} p_{ff}^2(\hat{\mathbf{r}}_\theta, m\Delta_t)}{\sum_{m=-\infty}^{\infty} p_i^2(m\Delta_t)}. \quad (20)$$

In all cases, the strongest scattering occurs at 180° back toward the source and the characteristic[7] scattering nulls at ±90° can also be observed. The main trends are that as the scattering volume is increased the scattering becomes stronger, more directional, and more selective in frequency. These three quantities are, respectively, quantified by the half-power (−3 dB) lobe width W around 180°, the backscattered power ratio $H(180°)$ and the Q-factor in frequency (the center frequency f_m divided by the half-power bandwidth). Figure 4 depicts the relationship between backscatter lobe width and scattering region outer radius r_0. The empirically fitted trend line follows $W = 35° \times \lambda/r_0$, showing that this backscatter directionality is inversely proportional to the dimensions of the scattering volume. Figure 5 depicts the relationship between backscattered power ratio and scattering region volume V_{scat} and the trend line follows $0.213 \times V_{\text{scat}}^2$. The values of $H(180°)$ which are greater than 1 occur because the scattered power was normalized to the incident power density, and $V_{\text{scat}} > 1\ \text{m}^3$. It is interesting therefore that scattered power scales with V_{scat}^2 instead of V_{scat}, since this implies the strength of the Bragg backscatter mechanism is also proportional to V_{scat}, though it must saturate at some volume since it is not possible to scatter more energy than is incident. Data for Q-factor is more limited. The data present in Table I appears to be inversely proportional to r_0, that is, a small scattering volume (including only a few periods of the temperature fluctuations) gives broadband backscatter whereas a large scattering volume (including many periods of the temperature fluctuations) gives backscatter which is quite narrowband and highly dependent on the spacing of the temperature fluctuations. For the smallest scattering volumes $r_0 = 0.15$ m and 0.3 m, Q could not be calculated since the frequency content of the backscatter was limited by the frequency content of the excitation, not by the frequency response of the backscattering process.

The second set of simulations examined the phase of the backscattered signal, since it has been established that this is important in remote sensing systems which utilize pulse compression.[21] Here the standard values for σ and r_0 were used and a number of simulations were run with small vertical shifts in the temperature profile defined by a random parameter $0 \le \alpha \le 2\pi$ with

$$T(\mathbf{r}) = T_0 + w(\mathbf{r})\cos(4\pi f_m \hat{\mathbf{z}}\cdot\mathbf{r}/c + \alpha)\Delta_T. \quad (21)$$

The phase of the reflection was examined at the excitation frequency and found to be equal to α to within 3 decimal places (plus a small constant offset of 4° caused by a delay

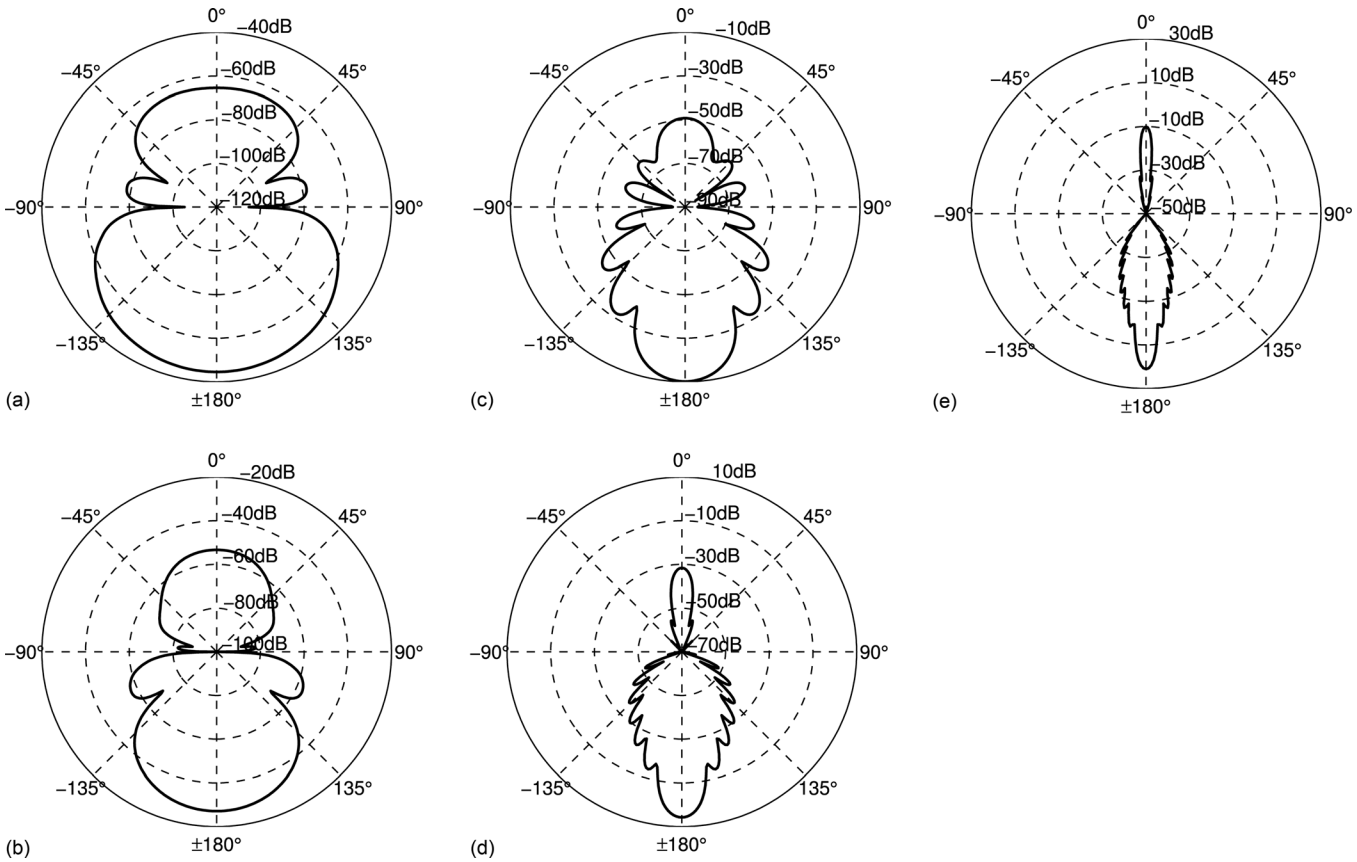

FIG. 3. Polar plots of far-field scattered power ratio $H(\theta)$ in dB versus angle for the "Bragg atmosphere" from smallest to largest scattering volume. (a) $r_0 = 0.15$ m, (b) $r_0 = 0.3$ m, (c) $r_0 = 0.6$ m, (d) $r_0 = 1.2$ m, (e) $r_0 = 2.4$ m.

factor). This is as expected since moving the temperature fluctuations amounts to changing the reflected path length and a delay (phase change in frequency) proportional to the increased path length will occur. This may seem like a trivial result; however, it will be drawn upon in the interpretation of the results in the next section.

B. Atmosphere with stochastic temperature fluctuations

In this section, an atmosphere with stochastic temperature fluctuations is modeled and the far-field scattering compared to theoretical results. There is insufficient space here to adequately describe the subtleties and motivations of the atmospheric models used, and the interested reader is directed toward Ref. 7 (Chap. 7) and Ref. 22 (Appendixes I and J), which provides a particularly accessible explanation.

It is assumed that the distribution of temperature fluctuations is homogeneous and isotropic, which is acceptable in a no-wind condition, and given by the Kolmogorov spectrum. Note that this differs from the study by Cheinet *et al.*[13] which used the von Karman spectrum. In three dimensions, the Kolmogorov spectral density as a function of wave number k is given by

TABLE I. Summary of far-field scattering by the "Bragg atmosphere." r_0 is the outer radius of the scattering region, V_{scat} is the volume of the scattering region, W is the half-power lobe width, $H(180°)$ is the backscattered power ratio, and Q is the Q-factor in frequency.

r_0 (m)	r_0/λ	V_{scat} (m^3)	W (deg)	$H(180°)$ (dB)	Q
0.15	0.44	0.0096	64.1	−44.5	-
0.30	0.88	0.077	38.8	−27.1	-
0.6	1.8	0.61	20.4	−10.1	5.55
1.2	3.5	4.90	10.2	5.77	11.0
2.4	7.1	39.2	5.13	21.1	21.8

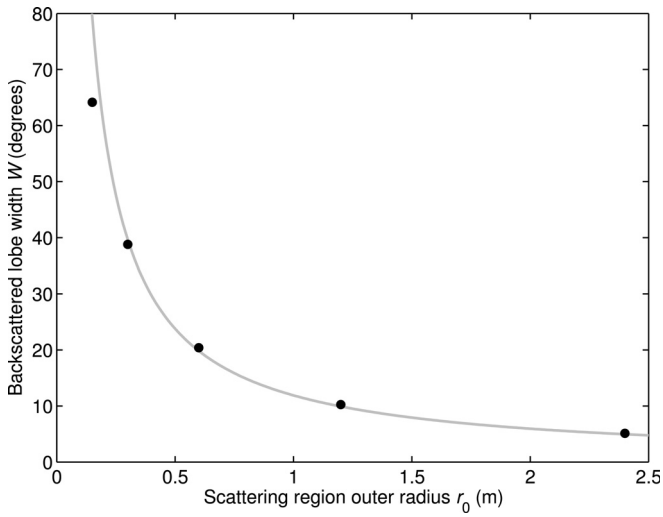

FIG. 4. Backscattered lobe width W versus scattering region outer radius r_0 for the "Bragg atmosphere."

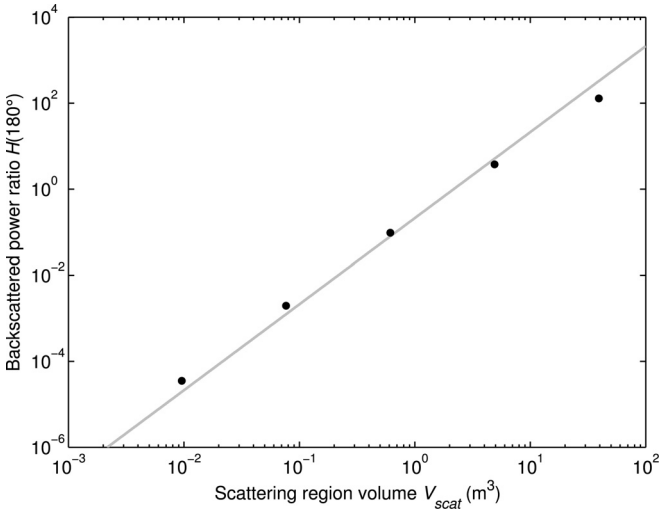

FIG. 5. Backscattered power ratio $H(180°)$ vs scattering region volume V_{scat} for the "Bragg atmosphere."

$$\Phi(k) = C_T^2 \frac{\Gamma(8/3)}{4\pi^2} \sin(\pi/3) k^{-11/3}. \tag{22}$$

Here C_T^2 is the temperature structure parameter and on a summer day it typically takes values in the range 2×10^{-10} m$^{-2/3}$ $\leq C_T^2/T_0^2 \leq 6 \times 10^{-7}m^{-2/3}$ (Ref. 7, Eq. 6.56). For the simulations herein, a value toward the upper limit of this range $C_T^2 = 1.5 \times 10^{-7} T_0^2$ (larger amplitude temperature fluctuations) has been used. Technically, this model is only valid within the range of characteristic eddy size $L_{\text{out}}^{-1} < k < L_{\text{in}}^{-1}$, termed the "inertial subrange," but this is not a problem as L_{out} is typically larger than the inhomogeneous domain V and L_{in} is smaller than the k-space grid spacing (and considered to be unimportant in acoustics[22]).

In what follows, it will be assumed that the temperature field (due to turbulence) is invariant during each SODAR pulse simulation; this amounts to a "frozen medium" approach and is valid where the rate of evolution of the temperature field is much lower than the speed of sound. Stochastic properties are characterized by generating multiple random instances of the temperature field and averaging their responses. The individual instances of the temperature field are generated from sampled versions of $\Phi(k)$ by applying a random phase (i.e., spatial offset) to each coefficient of the discretized spectrum and then applying a 3D inverse discrete Fourier transform; this is equivalent to the process described by Frehlich *et al.*[23] Note that for the Kolmogorov spectrum, the coefficient at $k = 0$ must be practically be omitted since $\Phi(0) = \infty$. The smallest and largest wave number components reconstructed were therefore 2π divided by the size of the modeling domain and 2π divided by the grid spacing, respectively.

Figure 6 depicts a slice through a temperature offset profile calculated by this method, including windowing by $w(\mathbf{r})$. As expected, there are rapidly varying features with small amplitude superimposed upon more slowly varying features with larger amplitude. The shape of the window $w(\mathbf{r})$ is also clearly visible. Temperature profile instances generated by this method will be referred to as "Kolmogorov atmospheres."

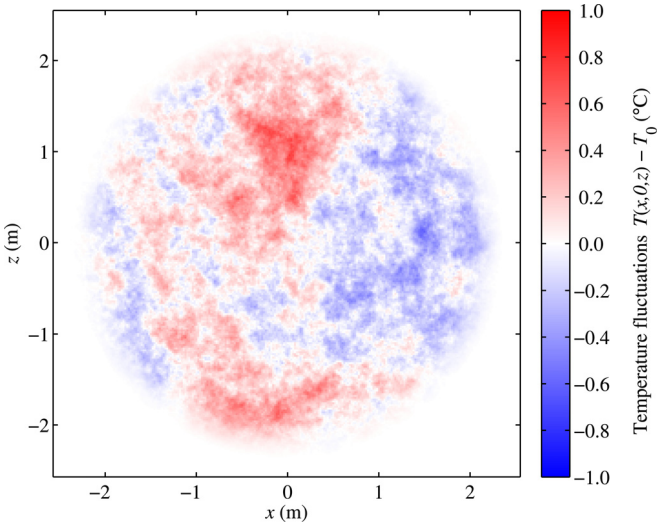

FIG. 6. (Color online) Slice through an instance of a temperature field (minus ambient) for an instance of a "Kolmogorov atmosphere."

Ostashev gives an analytical model for the scattering from stochastic atmospheres such as this in Sec. 7.1.3 of Ref. 7. Re-writing it for temperature fluctuations only gives

$$\sigma(\theta) = 0.0041 \frac{C_T^2}{T_0^2} \frac{k^{1/3} \cos^2\theta}{(\sin(\theta/2))^{11/3}}. \tag{23}$$

The quantity $\sigma(\theta)$ is the scattering cross-section per unit volume, and it is related to the scattered power ratio $H(\theta)$ by $H(\theta) \approx (4\pi)^2 V_{scat} \sigma(\theta)$. Figure 7 shows the analytical model superimposed on a set of numerical results. The gray lines are the scattering from eight independent temperature profile realizations; these are stochastically generated so unsurprisingly they have quite irregular scattering patterns. The dark black line is the power average of these measurements and shows a much more regular pattern. The dashed line is the scattering predicted by analytical model, showing good agreement both in scattering pattern and amplitude despite the

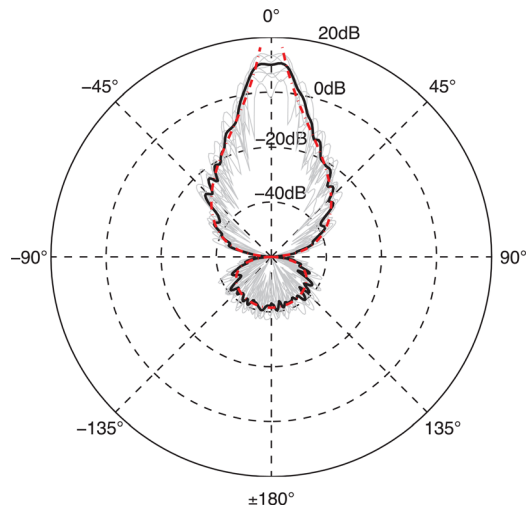

FIG. 7. (Color online) Polar plot of far-field scattered power ratio $H(\theta)$ in dB versus angle for the "Kolmogorov atmosphere." Gray lines are individual simulations, black line is the power average of these simulations, dashed line is the analytical model.

relatively small number of simulation instances which are averaged (Cheinet *et al.*[13] use 200 instances in an equivalent calculation). A major discrepancy is however seen for the forward scattering around $\theta = 0°$. Recall from Fig. 2 that a non-periodic temperature offset (i.e., with a spectrum that is large at small k) produces a significant forward-scatter to account for the change in sound speed encountered as the wave passes through the domain. The classical model of large scattering angle for the Kolmogorov spectrum is an extreme example of this; it predicts infinite scattering at $\theta = 0°$ due to the infinite temperature offset implied by $\Phi(0) = \infty$. This behavior is not replicated in the numerical results because the infinite value of $\Phi(0)$ was omitted from the turbulence reconstruction on the grounds of being unphysical. In addition, the windowing of the temperature fluctuations effectively imposes an L_{out} turbule size limit and significantly affects the forward scatter. A similar effect was seen for the von Karman spectrum by Cheinet *et al.*,[13] who go on to analyze the forward scattering case in much greater detail than is considered here.

The result at the end of Sec. III A demonstrated that spatially offsetting periodic temperature fluctuations causes a related change of phase in the backscattered sound. Since instances of the Kolmogorov atmosphere may be thought of as a sum of such fluctuations spatially offset by a random amount, it follows that the phase of different frequency components in the backscattered sound will also be independently random. In addition, the backscattered phase for the same frequency will vary randomly for different temperature field instances, for instance, during a SODAR measurement which is long with respect to the rate of evolution of the temperature field. Table II gives the phase of the signal backscattered from the eight simulated instances of the Kolmogorov atmosphere, both for $f_m = 1\,\text{kHz}$ and $f_m = 1.2\,\text{kHz}$ excitation; in the right hand columns, the corresponding relative delays have been calculated to permit easy comparison between the different frequency data. As expected there is no discernible relationship between the backscattered phases at 1 kHz and 1.2 kHz; they appear to be independently random.

This result has implications for the design of pulse-compression algorithms for SODAR, since the matched filtering they utilize depends on a linear-phase time-invariant response. This means backscattered delay must be equal over the operating bandwidth and time-invariant over each pulse sequence, and the discussion above and results in Table II shows that this is not the case. As discussed in Ref. 21, under these circumstances the benefits of the matched filtering are lost and the system performs no better than a non-coherent multi-frequency approach.

TABLE II. Phase (and equivalent delay) of backscatter from the "Kolmogorov atmosphere." Each row in the table presents the data from a different simulation instance.

Backscattered Phase		Relative Backscattered Delay	
1000 Hz	1200 Hz	1000 Hz	1200 Hz
−95.3°	−96.9°	−0.265 ms	−0.224 ms
−113.1°	−154.8°	−0.314 ms	−0.358 ms
−121.1°	−117.6°	−0.336 ms	−0.272 ms
23.1°	126.7°	0.064 ms	0.293 ms
−128.3°	−20.3°	−0.356 ms	−0.047 ms
62.8°	36.4°	0.175 ms	0.084 ms
89.5°	120.1°	0.249 ms	0.278 ms
87.8°	−117.5°	0.244 ms	−0.272 ms

IV. DISCUSSION, CONCLUSIONS, AND FUTURE DIRECTIONS

This paper has described a numerical method for simulating far-field scattering from small regions of inhomogeneous temperature fluctuations. The method combined an analytical incident sound model with a k-space model of the scattered sound close to the inhomogeneous region and a Near-to-Far-Field transformation to obtain far-field scattering patterns. The algorithm was applied to two idealized test case atmospheres: one with periodic temperature fluctuations with height and one with stochastic temperature fluctuations given by the Kolmogorov spectrum, for which good agreement with classical results was seen. From that perspective, this paper may be thought of as an extension of some aspects of the work of Cheinet *et al.*[13] to three dimensions. The paper also aimed to draw conclusions about multi-frequency SODAR performance and to that end the phase of the backscattered signals was analyzed. This suggested that stochastic atmospheres produce a randomized phase response which is independent with respect to frequency, suggesting atmospheric backscatter is an unsuitable target for matched-filter multi-frequency SODAR systems.

However, the model also has various limitations which require further discussion. One important aspect is that turbulent velocity fluctuations are omitted in this simulation (as they are in Sec. III B of Ref. 13). This was justified by citing the classical result that only temperature fluctuations contribute to the backscattered signal, but it would be desirable to properly test this assertion. With regard to the conclusions about randomized phase scattering from stochastic temperature fluctuations, it is conceivable that velocity fluctuations may have an additional effect (they are, for example, known to cause a widening of the Doppler peak), but it seems far more likely that this would create further phase randomization rather than remove it. Considering the full propagation path shown in Fig. 1, it is also clear that consideration has not been given to scattering processes between the SODAR and the scattering volume in either direction, and in a stochastic atmosphere these are also likely to be dispersive effects. It therefore seems reasonable to suppose that the stochastic features omitted from the model would further compromise the performance of the matched-filter post processing in a multi-frequency SODAR, so the negative conclusions reached here are likely to be generalizable.

As regards the suitability of the method as a numerical testbed for a broader class of SODAR, it is clear that the omitted features described in the previous paragraph would be also desirable for this application. Stochastic velocity fluctuations due to turbulence could be incorporated within the k-space model of the scattering region, though initial efforts suggest that this will be very computationally

expensive and probably require a GPGPU implementation. Another important extension would be to include temperature and wind profiles through the atmosphere. It is anticipated that these could be included by modifying only the incident and far-field parts of the model to account for the curvature those sound waves experience while propagating through the atmosphere, and that the *k*-space model of the scattering volume could be left largely unchanged (albeit perhaps cast into a moving coordinate system in the case of wind shear).

It would also be interesting to simulate the periodic temperature fluctuation scenario over many different cases over wider frequency bands, since it is essentially a building block of the stochastic atmosphere scenario. This may enable a better understanding of the scattering of sound by atmospheric turbulence and permit extraction of more trends, which could possibly even form the basis of an empirical model. However, the computation speed of the current code precludes this and a much faster implementation (e.g., GPGPU) would be necessary also to undertake this investigation.

The applicability of all these approaches, however, is built upon the validity of the Born approximation, which is essentially that forward scatter is negligible as a sound wave propagates through the atmosphere, meaning the backscatter from a small region may be calculated independently of the scattering from other regions. At first glance, Fig. 7 suggests that forward scattering is far from negligible, but as discussed in Sec. III B, the forward scatter predicted there is predominately associated with slight changes in the speed of sound due to spatially large temperature fluctuations. Hence, it is likely to be non-dispersive and to not have a significant effect on SODAR measurements. Given an adequate computational resource, it would be attractive to verify these assumptions by undertaking a small number of models of very large FDTD domains (themselves ideally verified against measurement), against which less computationally demanding algorithms (such as those proposed above) could ultimately be verified.

ACKNOWLEDGMENTS

This work was supported by the UK Engineering and Physical Sciences Research Council [grant number EP/G003734/1 "Advanced Signal Processing Methods Applied to Acoustic Wind Profiling for Use in Wind Farm Assessment"]. The authors thank also Jonathan Sheaffer for his constructive feedback on an early version.

[1]S. G. Bradley, *Atmospheric Acoustic Remote Sensing* (Taylor and Francis CRC Press, Florida, 2008), 328 pp.
[2]S. G. Bradley, "Use of coded waveforms for SODAR systems," Meteorol. Atmos. Phys. **71**, 15–23 (1999).
[3]A. Nagaraju, A. Kamalakumari, and M. Purnachandra Rao, "Application of pulse compression techniques to monostatic doppler SODAR," Glob. J. Res. Eng. **10**, 37–40 (2010). Available online at http://www.engineeringresearch.org/index.php/GJRE/article/view/53/52.
[4]T. J. Cox, "Acoustic iridescence," J. Acoust. Soc. Am. **129**, 1165–1172 (2011).
[5]V. I. Tatarski, *Wave Propagation in a Turbulent Medium* (Dover Publications Inc., New York, 1961), 285 pp.
[6]M. A. Kallistratova, "Backscattering and reflection of acoustic waves in the stable atmospheric boundary layer," IOP Conf. Ser. Earth Environ. Sci. **1**, 14 (2008).
[7]V. E. Ostashev, *Acoustics in Moving Inhomogeneous Media* (Spon Press, London, 1997), 259 pp.
[8]M. Legg, "Multi-frequency clutter-rejection algorithms for acoustic radars," Masters thesis, The University of Auckland, Auckland, Australia, 2007.
[9]B. Piper, S. Bradley, and S. von Hunerbein, "Calibration method principles for monostatic sodars," UPWIND Project Report (University of Salford, Manchester, UK, 2007).
[10]R. Blumrich and R. Heimann, "A linearized Eulerian sound propagation model for studies of complex meteorological effects," J. Acoust. Soc. Am. **112**, 446–455 (2002).
[11]V. E. Ostashev, D. K. Wilson, L. Liu, D. F. Aldridge, N. P. Symons, and D. Marlin, "Equations for finite-difference, time-domain simulation of sound propagation in moving inhomogeneous media and numerical implementation," J. Acoust. Soc. Am. **117**, 503–517 (2005).
[12]D. K. Wilson and L. Liu, *Finite-Difference, Time-Domain Simulation of Sound Propagation in a Dynamic Atmosphere* (US Army Corps of Engineers Engineer Research and Development Center, Hanover, NH, 2004).
[13]S. Cheinet, L. Ehrhardt, D. Juvé, and P. Blanc-Benon, "Unified modeling of turbulence effects on sound propagation," J. Acoust. Soc. Am. **132**(4), 2198–2209 (2012).
[14]R. J. Luebbers and M. Schneider, "A finite-difference time-domain near zone to far zone transformation," IEEE Trans. Ant. Prop. **39**, 429–433 (1991).
[15]A. Taflove and S. C. Hagness, *Computational Electrodynamics—The Finite Difference Time-Domain Method* (Artech House, Norwood, MA, 2005), 1038 pp.
[16]M. Tabei, T. D. Mast, and R. C. Waag, "A *k*-space method for coupled first-order acoustic propagation equations," J. Acoust. Soc. Am. **111**, 53–63 (2002).
[17]M. Hornikx, R. Waxler, and J. Forssén, "The extended fourier pseudospectral time-domain method for atmospheric sound propagation," J. Acoust. Soc. Am. **128**, 1632–1646 (2010).
[18]B. E. Treeby and B. T. Cox, "k-Wave: MATLAB toolbox for the simulation and reconstruction of photoacoustic wave-fields," J. Biomed. Opt. **15** 021314 (2010), http://www.k-wave.org/ (Last viewed 13 May 2013).
[19]X. Yuan, D. Borup, J. Wiskin, M. Berggren, and S. A. Johnson, "Simulation of acoustic wave propagation in dispersive media with relaxation losses by using FDTD method with PML absorbing boundary condition," IEEE Trans. Ultrason. Ferroelectr. Freq. Control **46**, 14–23 (1999).
[20]A. D. Pierce, *Acoustics: An Introduction to its Physical Principles and Applications* (Acoustical Society of America, New York, 1989).
[21]P. Kendrick and S. V. Hünerbein, "Pulse compression in SODAR," *16th International Symposium for the Advancement of Boundary-Layer Remote Sensing*, Boulder, CO (2012).
[22]E. M. Salomons, *Computational Atmospheric Acoustics* (Kluwer Academic Publisher, Boston, MA, 2001), 348 pp.
[23]R. Frehlich, L. Cornman, and R. Sharman, "Simulation of three-dimensional turbulent velocity fields," J. Appl. Meteorol. **40**(2), 246–258 (2001).